Robust Position Control of Dielectric Elastomer Actuators Based on LMI Optimization

Robust Position Control of Dielectric Elastomer Actuators Based on LMI Optimization

Gianluca Rizzello, David Naso, *Senior Member, IEEE*, Biagio Turchiano, *Senior Member, IEEE*, Stefan Seelecke

Abstract— **This paper develops a model based control strategy for a bi-stable positioning system based on a dielectric elastomer. The motion is generated by the electrostatic compressive force between two compliant electrodes applied on the surface of the elastomer. The membrane is connected to a bi-stable spring that acts as a biasing element and significantly extends the possible stroke. Such a design choice, however, makes the system strongly nonlinear and open-loop unstable. Starting from the extension of a dynamic model developed for a simpler version of the actuator, this paper proposes a strategy based on robust control design tools for linear parameter varying systems. The approach guarantees both stability and worst-case performance in the whole operating range of the system. Both simulations and experiments are used to assess the advantages of the proposed design method.**

***Index Terms*- Dielectric Elastomers, Dielectric Electro-Active Polymers, Mechatronics, Precision Motion Control, Robust Control, LPV, LMI.**

I. Introduction

DIELECTRIC Elastomers (DE's), also known as Dielectric Electro-Active Polymers, represent an innovative class of smart materials which exhibit relatively large deformations when solicited by an electric field [1]. DE's consist of a film of elastic polymeric material covered on both sides by compliant electrodes. When a voltage is applied to the electrodes, the resulting electric field generates a compressive stress that produces a controllable deformation of the film. This deformation can be in some cases one or two orders of magnitude larger than the one obtained by other smart materials (e.g., piezoelectric ceramics or shape memory alloys). This peculiarity, together with the low production cost, the low power requirement, and the comparatively high bandwidth, makes DE's an interesting alternative to develop innovative force and motion actuators.

A large part of recent literature on DE Actuators (DEA's) deals with static and dynamic characterization [2]–[4], and accurate modeling of the physical mechanism underlying material behavior [5]–[12]. From a macroscopic viewpoint, DEA's exhibit a complex dynamic behavior, often characterized by a relevant amount of nonlinearities and uncertainties. The possibility of using feedback control as a means to cope with those phenomena is receiving increasing attention in scientific literature. Most of the work performed in the last decade on the subject focused on standard solutions based on PID control. In [13], Xie *et al.* developed an embedded DEA sensing and actuation system where a PID law tuned with Zieglers-Nichols rules is used to control position and force of the device. In [14], Randazzo *et al.* explored the controllability of a rotational joint driven by two DEA's arranged in an antagonistic configuration, and implemented a closed loop PID control for regulating both angular position and force. In [15], Yun and Kim presented a model-based anti-windup digital PID designed directly in the discrete time domain for position control of a DEA. In [16], Rizzello *et al.* performed an investigation of potentialities of model-based PID control on a DEA mass-spring actuator, providing several analytical tuning rules. Reference [16] also showed that closed loop performance can be improved significantly if the PID is combined with a simple nonlinear element which compensates the quadratic nonlinearity related to the DEA transduction principle.

To overcome the limitations of PID control, recent literature also investigates the potentialities of nonlinear control on DEA devices. For instance, Sarban and Jones realized active vibration isolation with a tubular DEA by adopting several approaches such as internal model control with gain-scheduling [17], and with an adaptive feedforward controller [18]. In [19] Wilson *et al.* compared the performance of a biomimetic, cerebellar-inspired controller with a conventional adaptive control scheme on a DEA, showing how the first strategy outperforms the second one when the actuator characteristics change significantly. In [20] Druitt and Alici proposed an experimental investigation of intelligent control methodologies, comparing a fuzzy logic PD+I control and neurofuzzy Adaptive Neural Fuzzy Inference System control (ANFIS) with a conventional PID.

While most of the previous literature investigates substantially heuristic design or tuning approaches, this paper makes an attempt to develop a systematic method using recent tools developed in the area of robust control. In particular, the paper focuses on the control of an innovative miniaturized precise positioning system based on an annular DE membrane combined with a bi-stable spring. The combination of the DE with the bi-stable spring permits a much larger actuation stroke in comparison with other biasing elements such as linear springs or masses [16], [21], but the feedback control becomes much more challenging

The authors would like to acknowledge the support of Parker-Hannifin, BioCare Business Unit.

G. Rizzello, D. Naso and B. Turchiano are with the Department of Electrical and Information Engineering, Politecnico di Bari, Bari, IT (e-mail: gianluca.rizzello@poliba.it, david.naso@poliba.it, biagio.turchiano@poliba.it).

S. Seelecke is with the Department of Mechatronics, Universität des Saarlandes, Saarbrücken, DE (e-mail: stefan.seelecke@imsl.uni-saarland.de).

since the system exhibits multiple equilibrium points for a fixed input, resulting into local open-loop instability [4].

This paper starts by extending the model in [16] in order to incorporate the nonlinear effects introduced by the bi-stable preloading element. Subsequently, the controller design problem is addressed using tools from Linear Parameter Varying (LPV) control theory and Linear Matrix Inequalities (LMI) algorithms, which allow the nonlinearities to be treated in a robust fashion, achieving output regulation with guaranteed exponential convergence and minimized control effort. The reformulation of the nonlinearities as a LPV system and the use of LMI for feedback control design has been proven to be a viable strategy for other smart materials [22], [23], and this paper extends and refines these tools to the challenging case of multi-stable DEA systems.

The reminder of this paper is organized as follows. Section II introduces the model of the considered device, while Section III focuses on validation and parameter identification. Then, Section IV proves the boundedness of the system state variables, a condition that is instrumental to the development of the control law presented in Section V. Finally, Section VI validates the proposed techniques with various experiments, and Section VII provides concluding remarks.

II. Control-Oriented DEA Model

This section first describes the DEA considered in this paper, and then introduces a detailed dynamical model obtained by extending the ideas developed for simpler systems in [16]. Even though in this paper it will be mainly used for control design, the model grounds on a physics-based approach that makes it particularly useful also for other scopes, such as mechanical design optimization, prediction and simulation [11], [12], [24].

A. Actuator overview

The device considered in this paper is based on the circular DE membrane shown in Fig. 1. A sketch of the membrane in undeformed resting condition and in deformed configuration is shown in Fig. 2 (a) and (b), respectively. The DE is made with silicone material with proprietary composition produced by Parker-Hannifin. The outer frame and the inner circular plate are made of rigid plastic (depicted in green), while the intermediate annular ring is the DE silicone membrane (in gray). A biaxial pre-strain is also applied to the polymeric film. Compliant carbon-based electrodes (in black) are screen-printed on both sides of the membrane, so that the polymer is sandwiched between them. When a voltage is applied to the electrodes, it generates a pressure (known as Maxwell Stress [25]) that compresses the material in the thickness direction, producing a radial expansion and the subsequent actuation motion shown in Fig. 3.

In order to achieve a significant amount of stroke, the membrane requires a mechanical bias. The actuator's biasing system considered in this work consists of a combination of a Nonlinear Biasing Spring (NBS) and a Linear Biasing Spring (LBS) connected to the rigid central plate by means of a rigid spacer (depicted in light grey in Fig. 3). The mechanism based on the NBS+LBS permits the tuning of the out-of-plane stroke and force of the actuator, and expands significantly the operating range with respect to other design options considered in earlier literature, e.g., linear springs [16]. The use of nonlinear biasing elements does not represent the only possible solution to obtain a significant increase in stroke. For instance, in [26] it is shown that a large stroke can be also achieved by exploiting the snap-through instability of the DE membrane. In principle, our robust design approach can be extended to this type of operating mode by appropriate modification of the model, but the investigation of this possibility goes beyond the scopes of this paper. Fig. 4 shows a comparison of NBS-based and linear spring biasing actions. The figure compares the static force-displacement curves of the DE for 0 (blue) and 2.5 kV (red) with the force-displacement curve of the biasing system (black). It can be observed that the application of a voltage reduces the stiffness of the elastomer. Since at steady-state the DE and the biasing are in

Fig. 1. DE membrane picture.

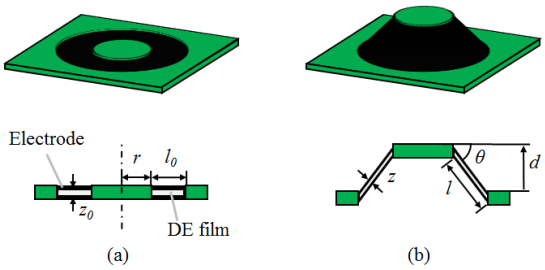

Fig. 2. DE membrane geometry in the undeformed (a) and deformed (b) configuration.

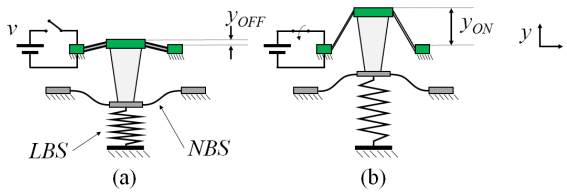

Fig. 3. Actuation mechanism, input voltage off (a) and on (b).

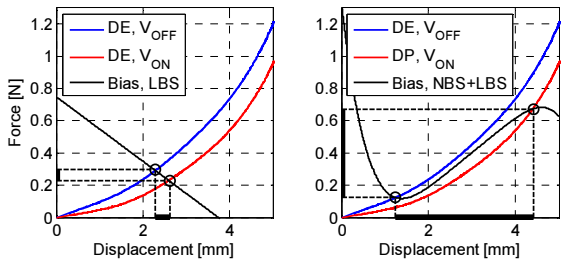

Fig. 4. DEA actuation stroke and force, for LBS load (left) and NBS+LBS load (right).

equilibrium conditions, the intersections between the curves determine the unactuated and actuated equilibrium points, and consequently the resulting actuation stroke and force.

B. Dynamical model

The model considers the voltage applied to the membrane v as input and the vertical displacement (or out-of-plane deflection) y as output (Fig. 3). The model is an extension of material developed for a simpler system described in [16]. Therefore, for brevity, in the following we only focus on the modifications necessary to capture the dynamical effects of the NBS. The first difference with respect to [16] consists in the biasing system, which now includes an extra NBS producing an additional NBS force F_{NBS} in the force equilibrium equation, given by

$$F_{NBS}(y) = \sum_{j=1}^{M} k_{nl,j}\left(y - y_n\right)^{c_j}, \tag{1}$$

where y_n is the NBS undeformed length, and M is the degree of the polynomial used to interpolate the experimental NBS characteristics. Moreover, in this paper the viscoelastic model is characterized in terms of average radial stretch and average radial stress, instead of the radial stress localized at inner radius. This can be performed by replacing the inner radius r with the average between inner and outer radii r_a, given by

$$r_a = \frac{2r + l_0}{2}, \tag{2}$$

when performing the conversion from DE force to radial stress. This modification does not affect the mathematical structure of the model, but it improves the ability to predict the motion of actuators with varying geometries [24]. The third and last difference consists in the viscoelastic model, which is now represented as a nonlinear spring, describing the quasi-static stress-stretch relationship, in parallel with a "capacitor element" representing the voltage-induced Maxwell stress, a dashpot and a spring-dashpot arm describing the material viscoelastic relaxation. A sketch of the spring-dashpot arrangement representing the viscoelastic model is given in Fig. 5, while the resulting state-space description of the overall viscoelastic dynamics is as follows:

$$\begin{cases} \dot{\varepsilon}_e = -\dfrac{k_e}{\eta_e}\varepsilon_e + \dfrac{k_e}{\eta_e}\left(\lambda_r - 1\right) \\ \sigma_r = -k_e\varepsilon_e + k_e\left(\lambda_r - 1\right) + \eta_p\dot{\lambda}_r + \sigma_e\left(\lambda_r\right) + \sigma_m\left(\lambda_r, v\right) \end{cases}, \tag{3}$$

where ε_e is an internal viscoelastic strain, λ_r and σ_r are the material radial stretch and stress, σ_e is the quasi-static elastic stress, σ_m is the Maxwell stress, and k_e, η_e and η_p represent stiffness and damping coefficients (see Fig. 5). Note that the time derivative of λ_r also appears in (3). However, this term can be rewritten as a function of the actuator displacement y and its time derivative, which are state variables of the overall state-space model. The complete model of the system is denoted as S, defined as follows:

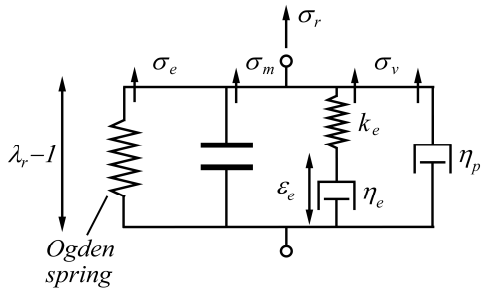

Fig. 5. Nonlinear viscoelastic model.

TABLE I
DEFINITION OF THE MAIN FUNCTIONS IN THE DEA MODEL

Function appearing in (4)

$$a = \frac{k_e}{\eta_e}$$

$$\lambda_r(x_2) = \sqrt{1 + \left(\frac{x_2}{l_0}\right)^2}$$

$$f(x_2) = \lambda_r(x_2) - 1$$

$$b(x_2) = \frac{2\pi r_a z_0 k_e}{l_0}\frac{x_2}{\lambda_r(x_2)^2}$$

$$k(x_2) = k_s\left(x_2 - y_l\right) + \sum_{j=1}^{M} k_{nj}\left(x_2 - y_n\right)^{c_j} + mg + \frac{2\pi r_a z_0}{l_0}\frac{x_2}{\lambda_r(x_2)^2}\left[\sum_{i=1}^{3}\left(\beta_i\lambda_r(x_2)^{\alpha_i} - \gamma_i\lambda_r(x_2)^{-\alpha_i}\right) + k_e f(x_2)\right]$$

$$c(x_2) = \frac{2\pi r_a z_0 \eta_p}{{l_0}^3}\frac{{x_2}^2}{\lambda_r(x_2)^3}$$

$$g(x_2) = \frac{2\pi r_a \varepsilon_0 \varepsilon_r}{z_0 l_0} x_2$$

$$S = \begin{cases} \dot{x}_1 = -ax_1 + af\left(x_2\right) \\ \dot{x}_2 = x_3 \\ \dot{x}_3 = \dfrac{b(x_2)}{m}x_1 - \dfrac{k(x_2)}{m} - \dfrac{c(x_2)}{m}x_3 + \dfrac{g(x_2)}{m}v^2 \\ y = x_2 \end{cases}, \tag{4}$$

where the state variable x_1 represents the internal viscoelastic strain (i.e. $x_1 = \varepsilon_e$) while x_2 and x_3 are the output displacement y and velocity $\dot{y}$. For completeness, the other terms appearing in (4) are reported in Table I, where the coefficients α_i, β_i, γ_i, i = 1, 2, 3 describe the Ogden model adopted to describe the material hyperelasticity, ε_0 and ε_r are the vacuum and DE permittivity, m is the mass of the spacer connecting the membrane to the springs, g is the gravitational acceleration, y_l is the LBS undeformed displacement, and the geometric parameters r_a, z_0 and l_0 represent the average between DEA inner and outer radii, and the thickness and radial length of the undeformed membrane, respectively.

III. Parameter Identification and Model Validation

The experimental bench for DEA testing is shown in Fig. 6, and consists of the DE membrane and its biasing system, a voltage amplifier (TREK 610E), a laser displacement sensor (Keyence LK-G37), a linear actuator used to modify the position of both springs with respect to the elastomer (Zaber T-NA08A25, indicated as Lin. Act. 1 in Fig. 6), and a linear actuator used to modify the relative position between the two loading springs (Zaber T-LA28A , indicated as Lin. Act. 2 in Fig. 6).

Several model parameters are known in advance, namely the ones related to the geometry and the biasing elements, and are reported in Table II. All the parameters describing the material electrical and mechanical properties, instead, require experimental identification. The first identification test aims to determine the coefficients affecting only the quasi static response, i.e. ε_r α_i, β_i, γ_i, i = 1, …, N. For this purpose, a linear actuator (Aerotech model ANT-25LA) is used to deform the DE membrane at 1 mHz and the resulting blocking force is measured with a load cell (Futek LSB-200). Once force and displacement measurements are available for different voltages, stress and strain are reconstructed by means of model equations, and the unknown coefficients are identified by using a least squares algorithm. The results of this identification are summarized in Table III. The overlap between the experimental and model behaviors is satisfactory (see Fig. 7). As in [16], a small hysteresis is introduced by the mechanical behavior of the compliant electrodes, but this phenomenon can be neglected. The experimental NBS force-displacement curve is shown in Fig. 8, together with the least-square best-fitting polynomial. The adopted polynomial has a maximum degree coefficient of order 15, and the number of coefficients has been reduced using standard optimization tools. A small hysteresis is observed nearby the area where the curve slope changes from positive to negative, as a consequence of the asymmetry in the snap mechanism producing the bi-stabile behavior.

For output regulation, we are interested in characterizing the low-frequency snapping mechanism of the system for different input voltages, so the identification of the remaining model parameters is performed using the sequence of step signals shown in Fig. 9. The voltage signal is applied when the actuator is pre-loaded with both y_l and y_n of 7 mm. Fig. 9 shows results of the system response and the consequent best-fit model output. The model is capable of predicting the effects of bi-stability, which are observable by comparing the different output values corresponding to an input of 2 kV. The values of the identified model coefficients are reported in Table III. Validation is performed for an input sinewave at 0.1 Hz and amplitude ranging from 0 to 2.5 kV, as shown in Fig. 10. The model is capable of reproducing the response and predict the nonlinearity introduced by the NBS. A small difference between experimental and simulated value of the initial displacement can be observed, as a consequence of the material creep, which results in a slowly varying drift of the DEA deformation. Including the description of slowly varying creep in the mathematical model would involve a

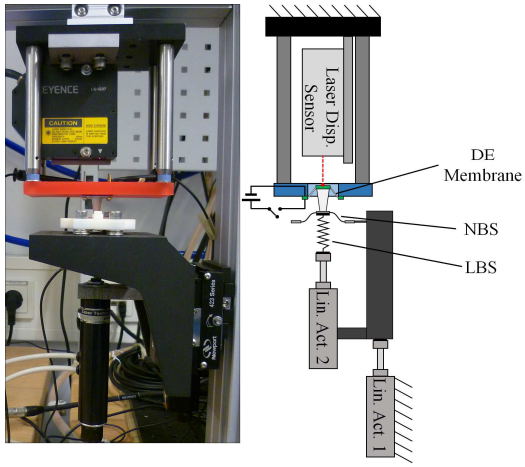

Fig. 6. DEA experimental setup, picture (left) and sketch (right).

significant overcomplication of its structure, and since its effects are not relevant for feedback control (it can be regarded as a slow disturbance which can be compensated by the integral part of the controller) the phenomenon will be neglected in this paper.

The use of the NBS also causes the bi-stable behavior observable in Fig. 11. The figure shows the input-output hysteresis simulated for a sinusoidal voltage at different frequencies, namely 0.1, 0.01, and 0.001 Hz. The typical hysteresis observed in DEA's is mainly due to the material viscoelasticity, while the hysteresis in Fig.11 is mainly due to the bi-stable behavior of the actuator, because when the input voltage ranges from 1.5 to 2 kV the system exhibits multiple equilibria.

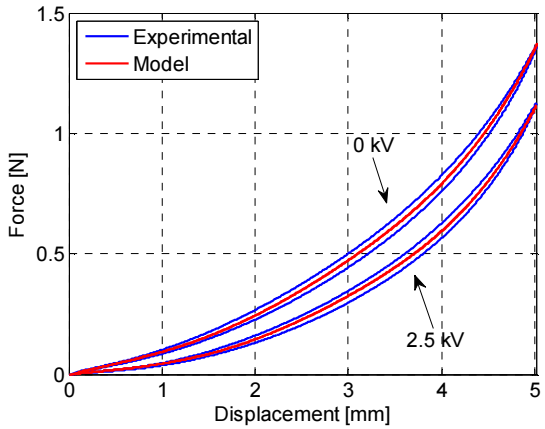

Fig. 7. Static DE identification, experimental (blue) and model (red).

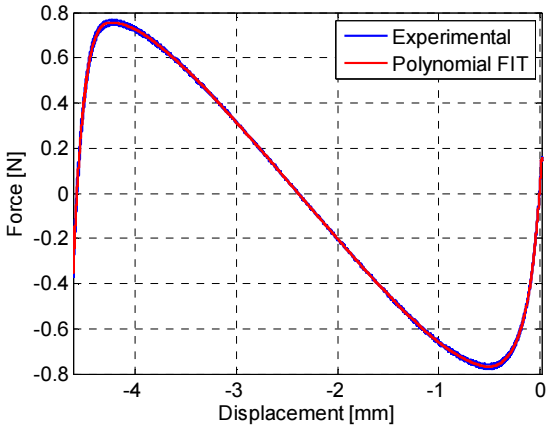

Fig. 8. NBS characteristics, experimental (blue) and Polynomial FIT (red).

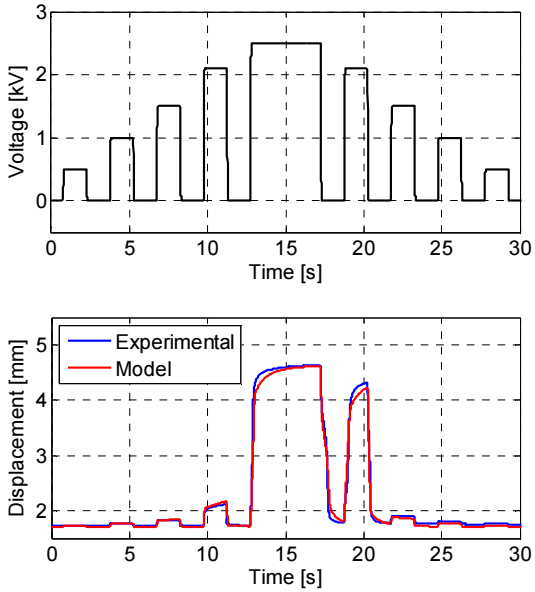

Fig. 9. Identification test, input (upper) and system response (lower), experimental, (blue) and model (red).

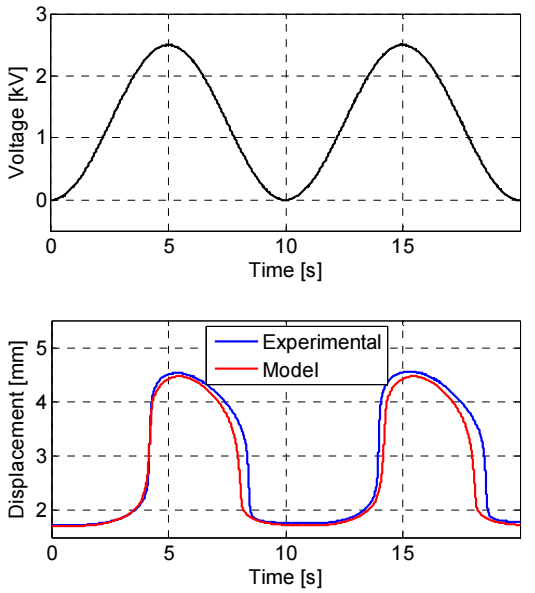

Fig. 10. Validation test, response for 0.1 Hz sinewave input, (blue) and model (red).

Fig. 11 also analyzes the local stability of such equilibria by evaluating the eigenvalue of the Jacobian matrix of the model (4) having the largest positive real part. In particular, for low input voltages, only one stable equilibrium exists (blue line in Fig. 11). When the voltage becomes larger than 1.5 kV, the system exhibits three equilibrium points, two stable (blue) and one unstable (red), while if the voltage exceeds a second threshold (2 kV), the system returns to exhibit only one stable equilibrium point (blue).

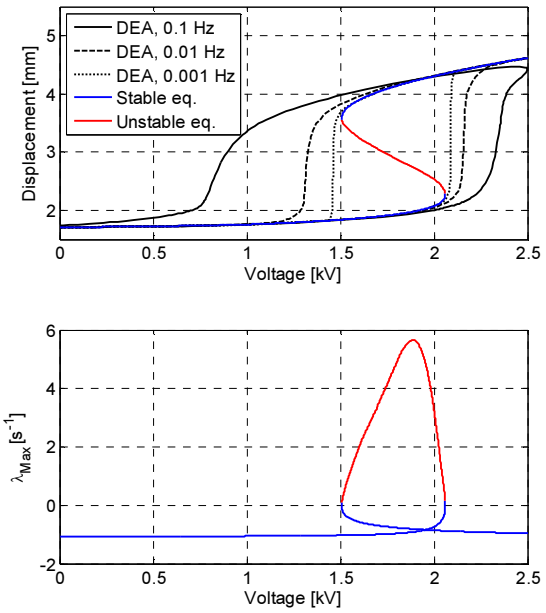

Fig. 11. DEA response for different frequencies and input-output equilibrium map (upper part), and corresponding eigenvalue of the Jacobian matrix with largest real part (lower part).

TABLE II
KNOWN MODEL PARAMETERS

Coefficient	*Symbol*	*Value*	*Unit*
DE membrane thickness	z_0	40	µm
DE membrane radial length	l_0	4.75	mm
DE membrane inner radius	r	6.25	mm
DE membrane average radius	r_a	8.625	mm
Vacuum permittivity	ε_0	$8.85 \cdot 10^{-12}$	F/m
Gravitational acceleration	g	9.81	m/s^2
Spacer mass	m	2.05	g
LBS stiffness	k_s	0.22	N/mm
LBS undeformed length	y_l	6.20	mm
NBS undeformed length	y_n	5.90	mm

TABLE III
IDENTIFIED MODEL PARAMETERS

Coefficient	*Symbol*	*Value*	*Unit*
Ogden model exponent	α_1	2	-
	α_2	4	-
	α_3	6	-
Ogden model stiffness	β_1	-2.15	MPa
	β_2	0.59	MPa
	β_3	0.11	MPa
	γ_1	-9.38	MPa
	γ_2	12.64	MPa
	γ_3	-4.89	MPa
DE membrane permittivity	ε_r	3.12	-
Viscoelastic model stiffness	k_e	0.40	MPa
Viscoelastic model series damping	η_e	0.35	MPa·s
Viscoelastic model parallel damping	η_p	0.03	MPa·s

IV. BOUNDEDNESS OF STATE VARIABLES

A necessary prerequisite to apply LPV techniques to our system is to ensure that the state variables remain bounded for a bounded input. The goal of this section is to prove that this occurs when some conditions are satisfied. This result will then be exploited in the next section devoted to control design.

We first consider a new dynamic system denoted as *S'* and defined by the second and third equations of (4)

$$S' = \begin{cases} \dot{x}_2 = x_3 \\ \dot{x}_3 = \dfrac{b(x_2)}{m}\upsilon_1 - \dfrac{k(x_2)}{m} - \dfrac{c(x_2)}{m}x_3 + \dfrac{g(x_2)}{m}{\upsilon_2}^2 \end{cases}. \quad (5)$$

System *S'* shares the same solutions of *S* in terms of $[x_2\ x_3]^T$, provided that the initial conditions are the same and the inputs are selected as $[\upsilon_1\ \upsilon_2]^T = [x_1\ v]^T$, with x_1 satisfying the first equation of *S*, and *v* chosen arbitrarily. Under these conditions, the projection of the trajectories of *S* on the $x_2 - x_3$ plane coincides with the trajectories of *S'*. Now let

$$\left[x_2(t)\quad x_3(t)\right]^T = \varphi\left(t, \left[x_2(0)\quad x_3(0)\right]^T, \left[\upsilon_1(\cdot)\quad \upsilon_2(\cdot)\right]^T\right) \quad (6)$$

be the state of *S'* at time *t* for initial condition $[x_2(0)\ x_3(0)]^T$ at time zero, and supposing that the input functions $[\upsilon_1(\cdot)\ \upsilon_2(\cdot)]^T$ are applied. Moreover, let

$$\begin{aligned} &\mathrm{T}\left(t, \left[x_2(0)\quad x_3(0)\right]^T, \left[\upsilon_1(\cdot)\quad \upsilon_2(\cdot)\right]^T\right) = \\ &= \left\{\varphi\left(t, \left[x_2(0)\quad x_3(0)\right]^T, \left[\upsilon_1(\cdot)\quad \upsilon_2(\cdot)\right]^T\right), t \geq 0\right\} \end{aligned} \quad (7)$$

indicate the corresponding trajectory obtained with inputs $[\upsilon_1(\cdot)\ \upsilon_2(\cdot)]^T$. We make the following assumptions.

Assumption 1)
The input of *S* is bounded,

$$v(t) \in [\underline{v}, \overline{v}], \forall t \geq 0. \quad (8)$$

Assumption 2)
There exist $\underline{x}_2$ and $\overline{x}_2$, with $0 < \underline{x}_2 < \overline{x}_2$, such that $\left[f(\underline{x}_2)\quad \underline{x}_2\quad 0\right]^T$ and $\left[f(\overline{x}_2)\quad \overline{x}_2\quad 0\right]^T$ represent equilibrium states of *S* corresponding to constant inputs $\underline{v}$ and $\overline{v}$, respectively. Obviously, $\left[\underline{x}_2\quad 0\right]^T$ and $\left[\overline{x}_2\quad 0\right]^T$ represent equilibrium states of *S'* corresponding to constant inputs $\left[f(\underline{x}_2)\quad \underline{v}\right]^T$ and $\left[f(\overline{x}_2)\quad \overline{v}\right]^T$.

Assumption 3)
After defining the quantities

$$\overline{\mathrm{T}} = \mathrm{T}\left(t, \left[\underline{x}_2\quad 0\right]^T, \left[f(\overline{x}_2)\quad \overline{v}\right]^T\right), \quad (9)$$

$$\underline{\mathrm{T}} = \mathrm{T}\left(t, \left[\overline{x}_2\quad 0\right]^T, \left[f(\underline{x}_2)\quad \underline{v}\right]^T\right), \quad (10)$$

$$\overline{\varphi} = \varphi\left(t, \left[\underline{x}_2\quad 0\right]^T, \left[f(\overline{x}_2)\quad \overline{v}\right]^T\right), \quad (11)$$

$$\underline{\varphi} = \varphi\left(t, \left[\overline{x}_2\quad 0\right]^T, \left[f(\underline{x}_2)\quad \underline{v}\right]^T\right), \quad (12)$$

we assume that states in $\overline{\mathrm{T}}$ and states in $\underline{\mathrm{T}}$ are such that

$$x_3 \geq 0 \ \ in\ \ \overline{\mathrm{T}}, \quad (13)$$

$$x_3 \leq 0 \ \ in\ \ \underline{\mathrm{T}}, \quad (14)$$

and moreover $\overline{\varphi}$ and $\underline{\varphi}$ are such that

$$\lim_{t\to\infty} \overline{\varphi} = \left[\overline{x}_2\quad 0\right]^T, \quad (15)$$

$$\lim_{t\to\infty} \underline{\varphi} = \left[\underline{x}_2\quad 0\right]^T. \quad (16)$$

The practical meaning of (13)-(16) is the following: if the system *S'* is at the equilibrium state $[\underline{x}_2\ 0]^T$ ($[\overline{x}_2\ 0]^T$) under constant inputs $\left[f(\underline{x}_2)\quad \underline{v}\right]^T$ ($\left[f(\overline{x}_2)\quad \overline{v}\right]^T$) and at $t = 0$ the inputs change to $\left[f(\overline{x}_2)\quad \overline{v}\right]^T$ ($\left[f(\underline{x}_2)\quad \underline{v}\right]^T$), the trajectory converges to the new equilibrium $[\overline{x}_2\ 0]^T$ ($[\underline{x}_2\ 0]^T$) with an overdamped transient response.

If (15)-(16) hold, the set $\overline{\mathrm{T}} \cup \underline{\mathrm{T}}$ defines a closed curve in the x_2 - x_3 plane (see Fig. 12). We denote Ω_{23} as the closed and bounded region of $\mathbb{R}^2$ delimited by this curve. We also define Ω as the closed and bounded region of $\mathbb{R}^3$ given by

$$\Omega = \left\{\left[x_1\quad x_2\quad x_3\right]^T \in \mathbb{R}^3 : x_1 \in \left[f(\underline{x}_2), f(\overline{x}_2)\right], \left[x_2\quad x_3\right]^T \in \Omega_{23}\right\}. \quad (17)$$

Under the previous assumptions, the following results can then be proved for *S*:

Proposition 1)
If

$$x_1(0) \in \left[f(\underline{x}_2), f(\overline{x}_2)\right] \quad (18)$$

and

$$x_2(t) \in [\underline{x}_2, \overline{x}_2], \forall t \in [0, t_1], \quad (19)$$

for any $t_1 > 0$, then

$$x_1(t) \in \left[f(\underline{x}_2), f(\overline{x}_2)\right], \forall t \in [0, t_1]; \quad (20)$$

Proposition 2)
If

$$\left[x_1(0)\quad x_2(0)\quad x_3(0)\right]^T \in \Omega, \quad (21)$$

then

$$\left[x_1(t)\quad x_2(t)\quad x_3(t)\right]^T \in \Omega, \forall t \geq 0. \quad (22)$$

Thus, under *Assumptions 1)-3)*, the closed set Ω represents a robust positive invariant set for system *S* [27]. A picture of the projection of this invariant set on the $x_2 - x_3$ plane, namely the region Ω_{23} delimited by $\overline{\mathrm{T}} \cup \underline{\mathrm{T}}$, is shown in blue line in Fig. 12, for $v \in [0, 2.5]$ kV and $x_2 \in [1.71, 4.62]$ mm. It can be observed that the trajectories satisfy the required assumptions. Moreover, $0 < \underline{x}_2 < \overline{x}_2$ as the membrane is elongating, implying that $f(x_2)$ is a monotonically increasing function in the operating range of interest.

Proof of Proposition 1. By inspection of the first state equation of *S*, it can be noted that it is equivalent to the cascade of the static nonlinearity $f(x_2)$ applied on x_2 and a stable LTI low-pass filter with unit static gain and a stable pole in $-a$. Since by (19) and *Assumption 2)* x_2 is positive, Table I implies that function $f(x_2)$ is monotonically increasing in the range $[\underline{x}_2, \overline{x}_2]$, making the proof of this proposition immediate.

Proof of Proposition 2. We define $\theta = [\theta_i \ \theta_j]^T$ as the unit vector tangent to the projection of the trajectories of *S* in the $x_2 - x_3$ plane, given by

$$\begin{bmatrix} \theta_i \\ \theta_j \end{bmatrix} = \begin{bmatrix} \dfrac{x_3}{\|\theta\|} \\ \dfrac{\dfrac{b(x_2)}{m} x_1 - \dfrac{k(x_2)}{m} - \dfrac{x(x_2)}{m} x_3 + \dfrac{g(x_2)}{m} v^2}{\|\theta\|} \end{bmatrix}, \quad (23)$$

where $||x||$ denotes the Euclidean norm of vector x. This unit vector varies according to the location on the $x_2 - x_3$ plane, as well as on the current values of the state variable x_1 and input v. The unit vector $\psi = [\psi_i \ \psi_j]^T$ normal to the border of Ω_{23} and pointing towards its interior is given by

$$\begin{bmatrix} \psi_i \\ \psi_j \end{bmatrix} = \begin{bmatrix} \dfrac{\dfrac{b(x_2)}{m} \upsilon_1 - \dfrac{k(x_2)}{m} - \dfrac{c(x_2)}{m} x_3 + \dfrac{g(x_2)}{m} \upsilon_2^2}{\|\psi\|} \\ -\dfrac{x_3}{\|\psi\|} \end{bmatrix}. \quad (24)$$

This unit vector depends on the particular point on the curve $\overline{\mathrm{T}} \cup \underline{\mathrm{T}}$ on the $x_2 - x_3$ plane, as well as on specific values of $[\upsilon_1 \ \upsilon_2]^T$ given by

$$\begin{bmatrix} \upsilon_1 & \upsilon_2 \end{bmatrix}^T = \begin{cases} \begin{bmatrix} f(\overline{x}_2) & \overline{v} \end{bmatrix}^T, \text{if } x_3 \geq 0 \quad (on \ \overline{\mathrm{T}}) \\ \begin{bmatrix} f(\underline{x}_2) & \underline{v} \end{bmatrix}^T, \text{if } x_3 < 0 \quad (on \ \underline{\mathrm{T}}) \end{cases}. \quad (25)$$

Note that the tangent vector (23) is generated by (4), while the normal vector (24) is given by the dynamical equations of (5). In order to prove that the projection of the trajectories of *S* on the x_2 - x_3 plane never escapes the region Ω_{23}, the angle between (23) and (24) must be within the range [-90, 90] degrees for every $[x_2 \ x_3]^T$ on $\overline{\mathrm{T}} \cup \underline{\mathrm{T}}$ and for every admissible v and x_1. This condition is equivalent to having the cosine of the angle between (23) and (24) always nonnegative, namely

$$\frac{\theta_i \psi_i + \theta_j \psi_j}{\|\theta\| \|\psi\|} \geq 0. \quad (26)$$

By replacing (23) and (24) into (26), we obtain

$$\frac{1}{m \|\theta\| \|\psi\|} x_3 \left[b(x_2)(\upsilon_1 - x_1) + g(x_2)(\upsilon_2^2 - v^2) \right] \geq 0. \quad (27)$$

From Table I, it is clear that $b(x_2)$ and $g(x_2)$ are always non-negative for positive x_2. Let us assume that the trajectories of *S* evolve starting inside Ω. Let us also assume that, for some $t_1 > 0$, the projection of system trajectory in the $x_2 - x_3$ plane touches the border of $\overline{\mathrm{T}} \cup \underline{\mathrm{T}}$. Now we consider two distinct cases:

1) The projection of the trajectory of *S* on the $x_2 - x_3$ plane reaches a point on $\overline{\mathrm{T}}$. On this branch, $x_3 \geq 0$, so (25), (8) and (20) imply (27). The trajectory projection is then pushed inside Ω_{23}, or it evolves on its border.
2) The projection of the trajectory of *S* on the $x_2 - x_3$ plane reaches a point on $\underline{\mathrm{T}}$. On this branch, $x_3 \leq 0$, so (25), (8) and (20) imply (27). The trajectory projection is then pushed inside Ω_{23}, or it evolves on its border.

This concludes the proof of *Proposition 2*.

For the DEA considered in this paper the input voltage is bounded in the range [0, 2.5] kV (according to *Assumption 1*). The bounds on x_1 and x_2 are immediately deducible from the equilibrium solutions of *S* under constant inputs $\underline{v}$ and $\overline{v}$, while the bounds on x_3 can be computed by generating $\overline{\mathrm{T}}$ and $\underline{\mathrm{T}}$. Considering the given parameters set and system input v confined to the closed interval $v \in [0, 2.5]$ kV, the resulting bounds are $x_1 \in [0.06, 0.4]$, $x_2 \in [1.71, 4.62]$ mm, $x_3 \in [-70.02, 85.21]$ mm/s. Fig. 12 draws in red line a simulated trajectory under a random-step input limited in the prescribed range, showing the satisfactory agreement between numerical and theoretical results.

It is worth mentioning that the proof given in this section

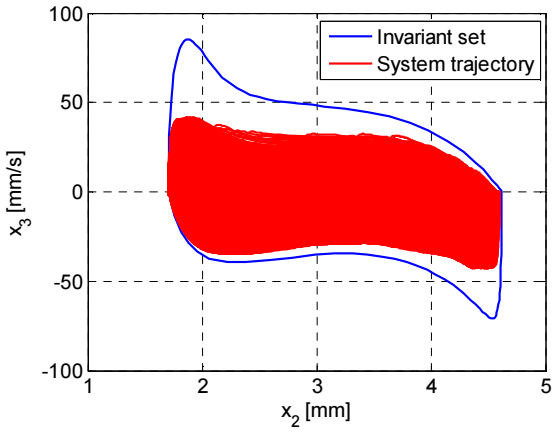

Fig. 12. DEA model invariant set on the $x_2 - x_3$ plane (blue), and system trajectory under a bounded input excitation (red).

can be easily extended for a the more general class of viscoelastic models which include an arbitrary number of parallel spring-dashpot arms, such as the model presented in [12]. Such an extension is quite straightforward, but for the sake of brevity is omitted from this work.

V. CONTROL DESIGN

The control goal is to achieve accurate regulation by robust compensation of the various nonlinearities affecting the developed model. In this paper we concentrate our attention on PID laws. Foreseeably, a control strategy based on model linearization, such as the one proposed in [16], will lead to controllers having satisfactory performance only around the linearization point. To overcome this limitation, this paper adopts the strategy of reformulating the DEA model as a LPV system and obtaining, by means of LMI optimization tools, a linear controller with guaranteed performances in the whole range of possible displacements.

A. DEA model as quasi-LPV system

By defining

$$p = \begin{bmatrix} x_1 \\ x_2 \end{bmatrix}, \tag{28}$$

and performing a few standard mathematical manipulations, it is easy to show that the second and third state equations in (4) can be viewed as a plant in the following quasi-LPV class [28]

$$\begin{cases} \begin{bmatrix} \dot{x}_2 \\ \dot{x}_3 \end{bmatrix} = \begin{bmatrix} 0 & 1 \\ \alpha_{21}(p) & \alpha_{22}(p) \end{bmatrix} \begin{bmatrix} x_2 \\ x_3 \end{bmatrix} + \begin{bmatrix} 0 \\ \beta_2(p) \end{bmatrix} u \\ y = \begin{bmatrix} 1 & 0 \end{bmatrix} \begin{bmatrix} x_2 \\ x_3 \end{bmatrix} \end{cases}, \tag{29}$$

where $\alpha_{21}(p)$, $\alpha_{22}(p)$ and $\beta_2(p)$ are continuous, differentiable functions of p, given by

$$\begin{cases} \alpha_{21}(p) = \dfrac{b(x_2)}{m x_2} x_1 - \dfrac{k(x_2)}{m x_2} \\ \alpha_{22}(p) = -\dfrac{c(x_2)}{m} \\ \beta_2(p) = \dfrac{g(x_2)}{m} \end{cases}. \tag{30}$$

We recall here the main result of Section IV, namely that there exist a subset Ω of $\mathbb{R}^3$ such that if $x(0) \in \Omega$ then $x(t) \in \Omega, \forall v \in [\underline{v}, \overline{v}]^T, \forall t \geq 0$. If we define

$$\Omega_{12} = \left\{ \begin{bmatrix} x_1 & x_2 \end{bmatrix}^T \in \mathbb{R}^2 : \exists x_3 \in \mathbb{R} \rightarrow \begin{bmatrix} x_1 & x_2 & x_3 \end{bmatrix}^T \in \Omega \right\}, \tag{31}$$

it holds that $p(t) \in \Omega_{12}, \forall t \geq 0$, thus we can establish bounds on p which depend on Ω. Since bounds for x_1 are known (see previous section) and the control of such unmeasurable variable is not of interest in our approach, it is more convenient to treat it as a bounded time-varying disturbance, and exploit the result obtained in the previous section. Moreover, it should be observed that for $x(t) \in \Omega$ the first function in (30) is well defined because x_2 is lower bounded by a positive value. We point out that also DEA's with higher order viscoelastic behavior (see e.g. [12]) can be described with the model in (29), provided that the output and all the viscoelastic states are embedded in the vector p. As remarked at the end of Section IV, the analysis of boundedness of state variables can be also performed for higher order viscoelastic models. In the case in which the bounds cannot be found analytically (e.g., when the DEA response is underdamped), it is still possible to estimate bounds on y from a significant set of simulations and then obtain the bounds on the viscoelastic states according to *Proposition 1)* in Section IV, or alternatively to perform numerical estimation of the invariant set (see e.g. [29]). Numerical estimation of bounds of p represents, indeed, the most common strategy suggested in literature about quasi-LPV systems, but this approach does not provide any guarantee that p remains within the bounds for every t.

The control input of the system (29) is defined as

$$u = v^2, \tag{32}$$

where v is the voltage applied to the electrodes. Obviously, the quadratic nonlinearity in the input voltage can be eliminated by inserting a square root function between the plant and the controller [16]. Note that the new input u is constrained to the range [0, 6.25] $(\text{kV})^2$, as a consequence of the limits on v.

B. Controller Design

Representing the dynamics of (4) as the quasi-LPV system (29) allows us to perform the design of a robust control law by using standard Linear Matrix Inequalities (LMI) optimization. The quasi-LPV system considers only x_2 and x_3 as state variables while, as mentioned, x_1 is regarded as a bounded time-varying disturbance. On the one hand, this leads to an increase in conservatism, since the correlation existing between the states and the parameters p is neglected. Therefore, if parameters p are assumed to be arbitrarily time-varying and bounded functions, the trajectories of the original system (4) are only a subset of all the possible trajectories of (29). On the other hand, the main advantage of the model reformulation in (29) is that the states (position and velocity) are completely accessible, and therefore it is suitable for implementing a state feedback control law resulting from LMI-based design. Moreover, since in most positioning applications zero steady-state error is required, an integral state x_i can be added to (29), obtaining the following augmented system

$$\begin{bmatrix} \dot{x}_i \\ \dot{x}_2 \\ \dot{x}_3 \end{bmatrix} = \begin{bmatrix} 0 & 1 & 0 \\ 0 & 0 & 1 \\ 0 & \alpha_{21}(p) & \alpha_{22}(p) \end{bmatrix} \begin{bmatrix} x_i \\ x_2 \\ x_3 \end{bmatrix} + \begin{bmatrix} 0 \\ 0 \\ \beta_2(p) \end{bmatrix} u. \tag{33}$$

In this way, the problem can be easily translated in error coordinates

$$e = \begin{bmatrix} e_i \\ e_p \\ e_d \end{bmatrix} = \begin{bmatrix} x_i \\ x_2 \\ x_3 \end{bmatrix} - \begin{bmatrix} \int_0^t y^* d\tau \\ y^* \\ \dot{y}^* \end{bmatrix}, \quad (34)$$

where y^* is the desired output. Differentiating (34) and substituting (33), we obtain that the dynamics of the tracking error is described in compact form by

$$\dot{e} = A(p)e + B(p)(u + \mu), \quad (35)$$

$$A(p) = \begin{bmatrix} 0 & 1 & 0 \\ 0 & 0 & 1 \\ 0 & \alpha_{21}(p) & \alpha_{22}(p) \end{bmatrix}, \quad (36)$$

$$B(p) = \begin{bmatrix} 0 \\ 0 \\ \beta_2(p) \end{bmatrix}, \quad (37)$$

$$\mu = \frac{\alpha_{21}(p)}{\beta_2(p)} y^* + \frac{\alpha_{22}(p)}{\beta_2(p)} \dot{y}^* - \frac{1}{\beta_2(p)} \ddot{y}^*. \quad (38)$$

The advantage of using the representation given by (35) is that a linear state feedback control for such system is given by

$$u = -Ke \equiv -k_i e_i - k_p e_p - k_d e_d, \quad (39)$$

that has the form of a PID control law, with

$$K = \begin{bmatrix} k_i & k_p & k_d \end{bmatrix}. \quad (40)$$

Replacing (39) in (35), the closed loop error dynamics is given by

$$\begin{cases} \dot{e} = \left[A(p) - B(p)K \right] e + B(p)\mu \\ u = -Ke \end{cases}, \quad (41)$$

whose closed loop state matrix is given by

$$A_{cl}(p) = A(p) - B(p)K. \quad (42)$$

System (41) is defined in such way that a suitable control performance can be defined in terms of some induced system norm from input μ to output u. In this paper we focus on set-point regulation, and assume that the desired output y^* is constant. As $\alpha_{21}(p)$, $\alpha_{22}(p)$ and $\beta_2(p)$ are constant for constant p, at the equilibrium one obtains

$$\begin{bmatrix} e_i \\ e_p \\ e_d \end{bmatrix} = \begin{bmatrix} \frac{\alpha_{21} y^*}{\beta_2 k_i} \\ 0 \\ 0 \end{bmatrix}, \quad (43)$$

which implies $e_p = 0$. In order to perform the design of K satisfying a certain specification, we assume that (41) can be represented as a polytopic model, namely that there exist constant matrices A_i and B_i, $i = 1,\ldots,V$, such that

$$\left[A(p)\ B(p) \right] \in conv\left\{ \left[A_1\ B_1 \right], \ldots, \left[A_V\ B_V \right] \right\}, \forall\ p \in \Omega_{12}. \quad (44)$$

The set of admissible $A(p)$ and $B(p)$ lies in the convex hull generated by the vertices matrices A_i and B_i, $i = 1,\ldots,V$. Sufficient conditions on stability for system (41) can then be proved only at the edges of the corresponding polytopic system [30]. Due to the nonlinear nature of the problem, in this work the vertices A_i, B_i are obtained by gridding $A(p)$ and $B(p)$ for a sufficiently large number of samples of p [31]. The design objective is to find the state feedback control law for model (35) in the form (39) such that the closed loop system satisfies the following specifications:

1) for a constant reference, the tracking error converges to zero not slower than a specified exponential decay rate α_D;
2) objective 1) is achieved with the minimum amount of control effort.

Condition 1) can be imposed by ensuring that

$$\exists \mathrm{M} > 0 : \left\| e(t) \right\| \le M \left\| e(0) \right\| \exp(-\alpha_D t), \forall t \ge 0. \quad (45)$$

The minimization of the control effort in 2) can be addressed by minimizing the $\mathcal{H}_2$ norm from μ to u. For SISO LPV systems, this is equivalent to minimize an upper bound of the ℓ_2 to ℓ_∞ gain from μ to u, also referred to as generalized $\mathcal{H}_2$ norm [32].

The design of state feedback controller ensuring both specifications can be stated in terms of a standard LMI eigenvalue problem [30]: find symmetric matrices P and Q and a rectangular matrix Y of appropriate dimensions which minimize

$$\gamma = Trace(Q), \quad (46)$$

and satisfy the following LMI constraints [30]:

$$P > 0, \quad (47)$$

$$A_i P + P A_i^T - B_i Y - Y^T B_i^T + 2\alpha_D P < 0, \forall i = 1,\ldots,V, \quad (48)$$

$$A_i P + P A_i^T - B_i Y - Y^T B_i^T + B_i B_i^T < 0, \forall i = 1,\ldots,V, \quad (49)$$

$$\begin{bmatrix} -Q & Y \\ Y^T & -P \end{bmatrix} < 0 \,. \tag{50}$$

Note that (47)-(48) correspond to specification 1), while (46), (49)-(50) correspond to specification 2). In order to simplify the computational complexity, the approach proposed here considers a constant matrix P, describing a parameter independent Lyapunov function. The LMI optimization is performed by means of the algorithms available in the *Matlab LMI Control Toolbox* environment [33]. The controller matrix K leading the desired specification is given by

$$K = YP^{-1} \tag{51}$$

Conditions (47)-(48) imply (45) only for autonomous system, while (41) contains also an external term μ depending on the reference signal y^*, and acting as an exogenous disturbance on the error dynamics. However, as first approximation we will neglect the effects of this term during the controller design, assuming that if the controller gains are sufficiently high the exogenous disturbance is efficiently compensated. One possible way to take into account the effects of the exogenous disturbance during the controller design is to include further LMI constraints to the problem in order to limit the effects of the disturbance on the tracking error, for instance by keeping the ℓ_2 to ℓ_∞ gain (generalized $\mathcal{H}_2$ norm) or ℓ_2 to ℓ_2 gain ($\mathcal{H}_\infty$ norm) from the disturbance to the tracking error below a certain level [34]. However, this possibility will not be explored in this paper.

VI. Results

The design procedure described in the previous section provides a PID control law in the form (39). Fig. 13 (a) shows the block diagram of the proposed control scheme, consisting in a standard PID in cascade with the static compensator of the quadratic nonlinearity.

The control law is implemented in discrete time with a sampling rate of 5 kHz and is executed in LabVIEW with a real-time FPGA data acquisition system. For the controller discretization, the Tustin rule was used for the integral action and the backward rectangular rule was used for the derivative action. As the DEA is essentially a capacitor, fast changes in the control voltage result in large spikes in the current which may eventually damage the actuator. For this reason, the derivative action in the PID law is calculated only on the system output. Moreover, every step reference is filtered with a first-order low-pass smoothing filter (denoted as SF in Fig. 13 (b)) with cut-off frequency of 10 Hz. Finally, the PID is implemented in an anti-windup back-calculation configuration [35]. The resulting modified controller scheme is shown in Fig. 13 (b).

In order to preliminarily assess the limitation of standard PID tuning methods such as those proposed in [16], Fig. 14 shows the simulation results of two PID's (including the compensation of the quadratic nonlinearity proposed in [16]) tuned on the linearized model at two different equilibria, namely

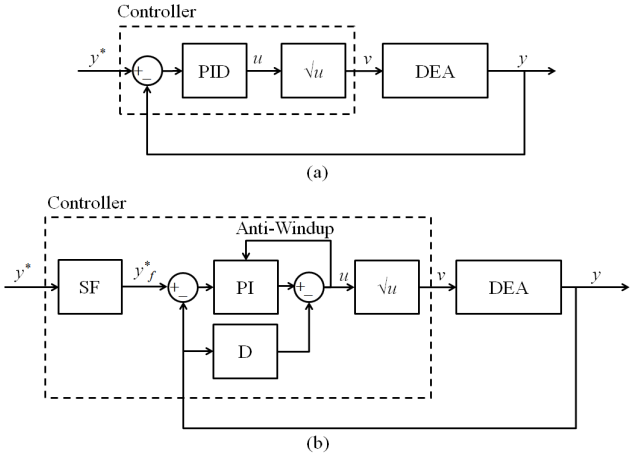

Fig. 13. PID controller with nonlinear compensation (a) and modified controller scheme for experimental implementation (b).

y = 1.71 mm (the minimum displacement) and y = 2.74 mm (the displacement corresponding to the equilibrium whose linearized transfer function exhibits the eigenvalue with the largest positive real part). The PID tuned on the model linearized at 1.71 mm is designed with the strategy proposed in [16]. Since for the second equilibrium point the linearized plant is open loop unstable, the method in [16] (based on pole-zero cancellation) cannot be applied. Therefore, the second PID is designed with a standard root locus technique with the goal of a settling time comparable with the one of LMI-based design. Fig. 14 shows that the performance of both controllers is satisfactory around the corresponding linearization point but becomes unsatisfactory (excessively under- or over-damped) for the other equilibrium point. Clearly, both controllers can be further tuned by hand to improve the global performance, but in any case such a heuristic approach lacks the guarantees of robust stability and performance offered by the design method considered in this paper.

The design of the robust PID's is performed by choosing different decay rates α_D as performance specification. Fig. 15 - Fig. 17 compare the closed loop performance obtained in simulation (blue) and on the experimental setup (red) with the response of a first order filter with a unit static gain and a

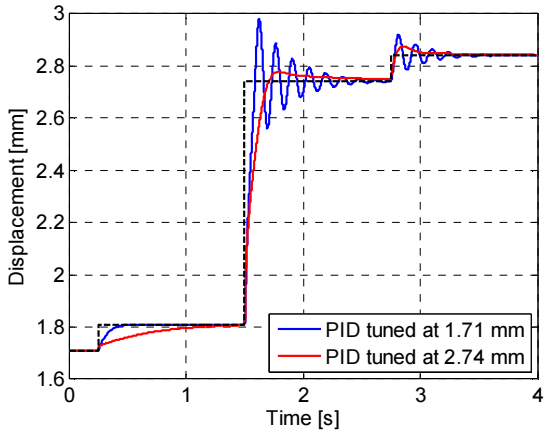

Fig. 14. Closed loop performance of two PID controllers tuned for different operating points, y = 1.71 (blue) mm and y = 2.74 mm (red). Both controllers perform well around the corresponding linearization point but tend to be unsatisfatory for the other operation point.

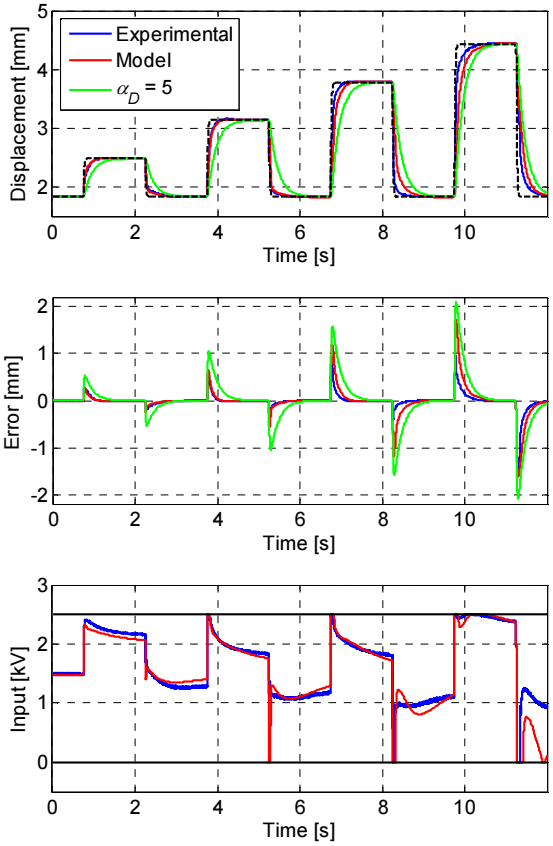

Fig. 15. Response of the controller to a square wave of increasing amplitude, experimental (blue), model (red), and response of a first order linear filter with unit static gain and pole in $-\alpha_D$ representing the decay rate specification (green), $\alpha_D = 5$.

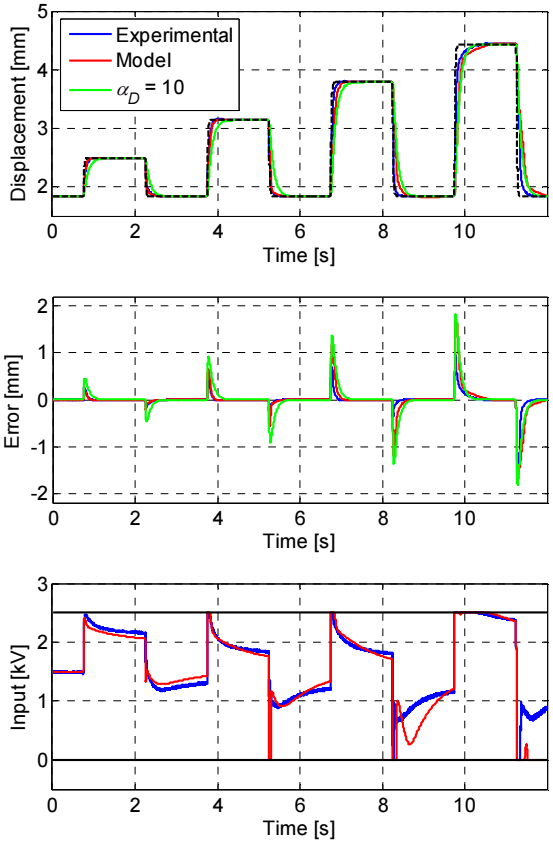

Fig. 16. Response of the controller to a square wave of increasing amplitude, experimental (blue), model (red), and response of a first order linear filter with unit static gain and pole in $-\alpha_D$ representing the decay rate specification (green), $\alpha_D = 10$.

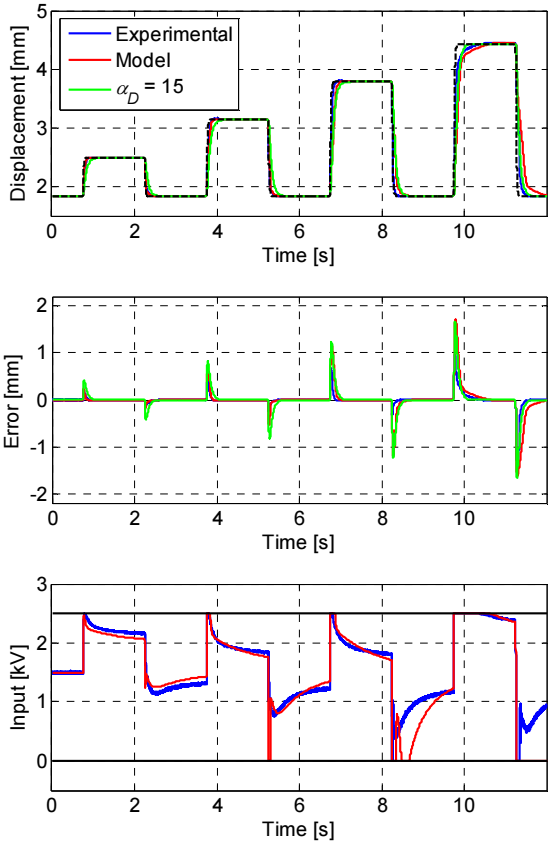

Fig. 17. Response of the controller to a square wave of increasing amplitude, experimental (blue), model (red), and response of a first order linear filter with unit static gain and pole in $-\alpha_D$ representing the decay rate specification (green), $\alpha_D = 15$.

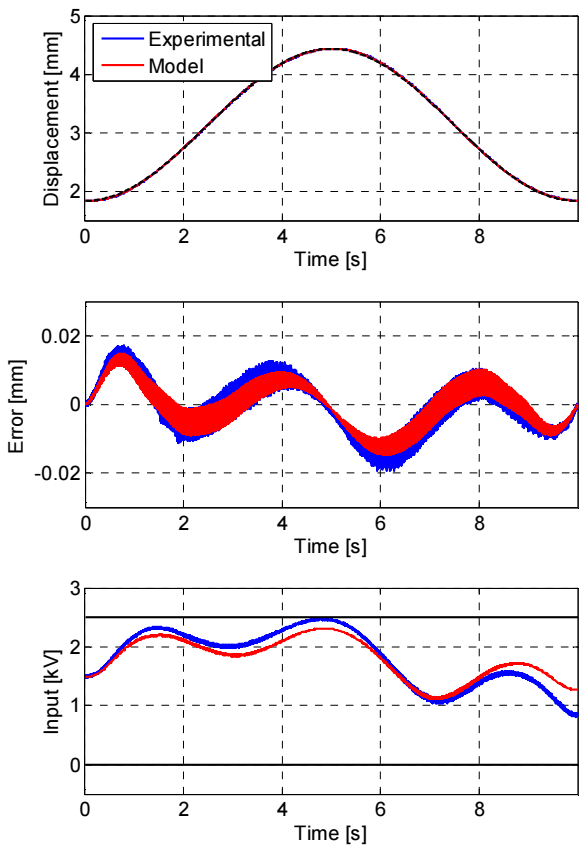

Fig. 18. Response of the controller to a 0.1 Hz sinewave, experimental (blue), and model (red), $\alpha_D = 15$.

pole in $-\alpha_D$ (in green), representing the decay rate specification. The control performance are compared for each test in terms of system output, tracking error and control input.

The PID gains depend on the chosen decay rate. Gradually increasing the decay rate generally makes the closed loop system faster, until some undesired phenomena such as oscillations or control input saturation start to appear. The decay rate must be chosen in order to achieve a satisfactory trade-off between these conflicting effects. Fig. 15 - Fig. 17 report the results for three values of decay rate (α_D = 5, 10, 15), and show that the experimental performance remains always within the specified bounds. The inspection of the first three steps in each figure shows that the controller needs to decrease the voltage in order to increase displacement, as a consequence of the bi-stability. Note that some of the set-point values represent equilibrium points which were unstable for the open loop system. For these particular cases, the resulting gains are high enough to compensate the effects of the exogenous term μ in the error dynamics (41), and no additional LMI constraints are required to meet the time-domain specification. Fig. 18 shows the results for the α_D = 15 controller in tracking a unipolar sinewave at 0.1 Hz. It can be noted that the controller allows us to stabilize every position in the actuation range, even the ones lying inside the hysteresis loop which were unstable for the open-loop system. Similar results are obtained with the other controllers. Table IV finally summarizes the controller gains k_p, k_i and k_d in the reported tests.

TABLE IV.
PID CONTROLLERS COEFFICIENTS, DESIGNED VIA LMI.

α_D	k_p	k_i	k_d
5	10.035	70.763	0.013
10	11.325	151.550	0.014
15	12.590	241.055	0.015

VII. CONCLUSIONS

This paper has focused on modeling and position control of a bi-stable DEA. The developed model has shown good ability in predicting the bi-stable behavior of the actuator for nonlinear biasing elements, and has been used to perform model-based control design by means of LMI optimization tools. Several simulations and experiments have been performed to validate the proposed approach. The system always settles to a constant set-point with the same velocity imposed by the specified decay rate, and the control system is able to hold any position within the actuator operating range, including the open-loop unstable ones. The approach is conservative, but it allows us to take into account explicitly of all the model nonlinearities, thus overcoming the limitations of a design method based on model linearization. Moreover, the resulting controller structure has the form of a PID, which is attractive for real-time implementation purposes. In summary, the proposed approach appears to be a viable strategy to address the design of linear controller for bi-stable DEA, effectively overcoming the problem deriving from the unmeasurable state variables, which also affects many other applications of smart materials. Finally, we remark that the modeling framework developed in [16] and extended here can be easily applied to other DEA configurations, making the proposed control technique a systematic, robust PID design method for a large class of DEA systems.

As the nonlinearities have been treated as uncertainties, the system tends to increase or decrease the response velocity depending on the selected set points. Future developments of this research will be devoted to investigate further approaches based on the LPV framework such as partial state feedback methods that do not consider the viscoelastic states as unknown disturbances, and LPV gain-scheduling based on parameter-dependent Lyapunov functions.

ACKNOWLEDGMENT

The authors wish to thank Dr. Alexander York for his help with laboratory setup, the associate editor and the reviewers for their constructive suggestions.

REFERENCES

[1] Y. Bar-Cohen, “Electroactive Polymers as Artificial Muscles - Reality and Challenges,” *Handb. biomimetics*, vol. 8, 2000.

[2] J. S. Plante and S. Dubowsky, “On the performance mechanisms of Dielectric Elastomer Actuators,” *Sensors Actuators, A Phys.*, vol. 137, no. 1, pp. 96–109, Jun. 2007.

[3] A. York, J. Dunn, and S. Seelecke, “Experimental characterization of the hysteretic and rate-dependent electromechanical behavior of dielectric electro-active polymer actuators,” *Smart Mater. Struct.*, vol. 19, no. 9, p. 094014, Aug. 2010.

[4] M. Hodgins, A. York, and S. Seelecke, “Modeling and experimental validation of a bi-stable out-of-plane DEAP actuator system,” *Smart Mater. Struct.*, vol. 20, no. 9, p. 094012, Aug. 2011.

[5] G. Kofod, P. Sommer-Larsen, R. Kornbluh, and R. Pelrine, “Actuation Response of Polyacrylate Dielectric Elastomers,” *J. Intell. Mater. Syst. Struct.*, vol. 14, no. 12, pp. 787–793, Dec. 2003.

[6] C. M. Hackl, H. Tang, S. Member, R. D. Lorenz, and L. Turng, “A Multidomain Model of Planar Electro-Active Polymer Actuators,” *IEEE Trans. Ind. Appl.*, vol. 41, no. 5, pp. 1142–1148, Sep. 2005.

[7] W. Kaal and S. Herold, “Electroactive Polymer Actuators in Dynamic Applications,” *IEEE/ASME Trans. Mechatronics*, vol. 16, no. 1, pp. 24–32, Feb. 2011.

[8] G. Berselli, R. Vertechy, M. Babic, and V. Parenti Castelli, “Dynamic modeling and experimental evaluation of a constant-force dielectric elastomer actuator,” *J. Intell. Mater. Syst. Struct.*, vol. 24, no. 6, pp. 779–791, Aug. 2013.

[9] G. Rizzello, D. Naso, and S. Seelecke, “A Nonlinear Electro-Mechanical Model for an Annular Dielectric Elastomer Actuator with a Biasing Mass,” in *VDI Tagung Mechatronik*, 2013, pp. 117–122.

[10] G. Moretti, M. Fontana, and R. Vertechy, “Modeling and control of lozenge-shaped dielectric elastomer generators,” in *ASME 2013 Conference on Smart Materials, Adaptive Structures and Intelligent Systems*, 2013, p. V001T03A039.

[11] M. Hodgins, G. Rizzello, D. Naso, Y. A, and S. Seelecke, “An electro-mechanically coupled model for the dynamic behavior of a dielectric electro-active polymer actuator,” *Smart Mater. Struct.*, vol. 23, no. 10, p. 104006, Sep. 2014.

[12] G. Rizzello, M. Hodgins, D. Naso, A. York, and S. Seelecke, “Modeling of the effects of the electrical dynamics on the electromechanical response of a DEAP circular actuator with a mass-spring load,” *Smart Mater. Struct.*, vol. 24, no. 9, p. 094003, 2015.

[13] S. Q. Xie, P. F. Ramson, D. Graaf, E. P. Calius, and I. A. Anderson, “An Adaptive Control System for Dielectric Elastomers,” in *2005 IEEE International Conference on Industrial Technology*, 2005, pp. 335–340.

[14] M. Randazzo, M. Fumagalli, G. Metta, and G. Sandini, “Closed loop control of a rotational joint driven by two antagonistic dielectric elastomer actuators,” in *SPIE Smart Structures and Materials+*

Nondestructive Evaluation and Health Monitoring, 2010, p. 76422D.
[15] K. Yun and W. Kim, "Microscale position control of an electroactive polymer using an anti-windup scheme," *Smart Mater. Struct.*, vol. 15, no. 4, p. 924, May 2006.
[16] G. Rizzello, D. Naso, A. York, and S. Seelecke, "Modeling, Identification, and Control of a Dielectric Electro-Active Polymer Positioning System," *IEEE Trans. Control Syst. Technol.*, vol. 23, no. 2, pp. 632–643, Mar. 2015.
[17] R. W. Jones and R. Sarban, "Inverse grey-box model-based control of a dielectric elastomer actuator," *Smart Mater. Struct.*, vol. 21, no. 7, p. 075019, Jun. 2012.
[18] R. Sarban and R. W. Jones, "Physical model-based active vibration control using a dielectric elastomer actuator," *J. Intell. Mater. Syst. Struct.*, vol. 23, no. 4, pp. 473–483, Feb. 2012.
[19] E. D. Wilson, T. Assaf, M. J. Pearson, J. M. Rossiter, S. R. Anderson, and J. Porrill, "Bioinspired Adaptive Control for Artificial Muscles," in *Biomimetic and biohybrid systems*, 2013, pp. 311–322.
[20] C. M. Druitt and G. Alici, "Intelligent Control of Electroactive Polymer Actuators Based on Fuzzy and Neurofuzzy Methodologies," *IEEE/ASME Trans. Mechatronics*, vol. 19, no. 6, pp. 1951–1962, Dec. 2014.
[21] M. Hodgins, A. York, and S. Seelecke, "Experimental comparison of bias elements for out-of-plane DEAP actuator system," *Smart Mater. Struct.*, vol. 22, no. 9, p. 094016, Aug. 2013.
[22] H.-H. Lin, B.-K. Fang, M.-S. Ju, and C.-C. K. Lin, "Control of Ionic Polymer-Metal Composites for Active Catheter Systems via Linear Parameter-Varying Approach," *J. Intell. Mater. Syst. Struct.*, vol. 20, no. 3, pp. 273–282, 2008.
[23] L. Riccardi, D. Naso, B. Turchiano, and H. Janocha, "Design of Linear Feedback Controllers for Dynamic Systems With Hysteresis," *IEEE Trans. Control Syst. Technol.*, vol. 22, no. 4, pp. 1268–1280, Jul. 2014.
[24] S. Hau, A. York, and S. Seelecke, "Performance prediction of circular dielectric electro-active polymers membrane actuators with various geometries," in *SPIE Smart Structures and Materials+ Nondestructive Evaluation and Health Monitoring*, 2015, p. 94300C.
[25] J. A. Stratton, *Electromagnetic Theory*. Wiley, John & Sons, Incorporated, 2007.
[26] H. Stoyanov, M. Kollosche, S. Risse, R. Waché, and G. Kofod, "Soft conductive elastomer materials for stretchable electronics and voltage controlled artificial muscles.," *Adv. Mater.*, vol. 25, no. 4, pp. 578–83, Jan. 2013.
[27] F. Blanchini and S. Miani, *Set-theoretic methods in control*. Springer Science & Business Media, 2008.
[28] J. Shamma, "An overview of LPV systems," in *Control of linear parameter varying systems with applications*, Springer, 2012, pp. 3–26.
[29] M. Dellnitz and O. Junge, "Set oriented numerical methods for dynamical systems," *Handb. Dyn. Syst.*, vol. 2, pp. 221–264, 2002.
[30] S. Boyd, L. El Ghaoui, E. Feron, and V. Balakrishnan, *Linear Matrix Inequalities in System and Control Theory*. SIAM, 1994.
[31] F. Amato, *Robust control of linear systems subject to uncertain time-varying parameters*. Springer, 2006.
[32] L. El Ghaoui and S.-I. Niculescu, *Advances in Linear Matrix Inequality Methods in Control*. SIAM, 2000.
[33] P. Ghainet, A. Nemirovski, A. Laub, and M. Chilali, "LMI Control Toolbox-for Use with Matlab," *Math Work. Inc*, 1995.
[34] C. Scherer, P. Gahinet, and M. Chilali, "Multiobjective output-feedback control via LMI optimization," *IEEE Trans. Automat. Contr.*, vol. 42, no. 7, pp. 896–911, Jul. 1997.
[35] K. J. Astrom, *PID controllers: theory, design and tuning*. Instrument society of America, 1995.